



Improvement in high-rate dischargeability, activation, and low-temperature performance in multi-phase AB₂ alloys by partial substitution of Zr with Y

K. Young^{a,*}, M. Young^b, T. Ouchi^a, B. Reichman^a, M.A. Fetcenko^a

^a Ovonic Battery Company, 2983 Waterview Drive, Rochester Hills, MI 48309, USA

^b Department of Electrical Engineering, Princeton University, NJ 08540, USA

H I G H L I G H T S

- Incorporation of Y in two AB₂ alloys and their electrochemical properties were studied.
- Both the high-rate dischargeability and activation are much improved.
- Large decrease in the surface charge transfer resistance was found at −40 °C.
- Both the C15 phase and Y-containing secondary phases are sources of the improvement.

A R T I C L E I N F O

Article history:

Received 13 April 2012

Received in revised form

11 May 2012

Accepted 12 May 2012

Available online 18 May 2012

Keywords:

Absorbing materials

Transition metal alloys

Metal hydride electrode

Electrochemical reactions

Laves phase

Multi-phase inter-metallic

A B S T R A C T

The changes in structure, gaseous phase hydrogen storage, and electrochemical properties due to the incorporation of Y in the alloy formula have been studied on two series of AB₂ alloys, with an originally C14- (relatively higher Cr-content) and a C15- (relatively higher Co-content) predominated micro-structure, respectively. In each series, 1–4 at.% of Y was added to the designed formula and partially replaced Zr. A majority of the added Y went into the secondary phases, such as YNi, (Y, Sn)-rich, and Y₂O₃, and only a small amount being found in the main AB₂ phase. The lattice constants and the unit cell volume decreased due to the reduction in Zr-content. The C15 phase abundances of the Y-containing alloys were higher than those of the Y-free alloys in both series. As the Y-content increased, the gaseous phase hydrogen storage capacity measured at 30 °C decreased in the high-Cr series and increased in the high-Co series. Both the hydrogen mid-point pressures and the electrochemical discharge capacities of the Y-containing alloys were lower than those in the Y-free alloys in both series. Both the activation and high-rate dischargeability (HRD) improved with the increase in Y-content. The −40 °C resistance was substantially reduced with the incorporation of Y in both series.

© 2012 Elsevier B.V. All rights reserved.

1. Introduction

The family of Laves phase-based AB₂ alloys is an alternative metal hydride (MH) electrode material designed to replace the rare-earth element-based AB₅ alloys in the nickel/metal hydride (Ni/MH) battery due to its higher capacity and comparatively lower raw material cost. The multi-phase nature of AB₂ alloys allows for the incorporation of many elements. The electrochemical properties of the alloy can be tailored by the selection of substitution elements. Most of the elements used in composition modification/optimization occupy the B-site, with examples such as B, Al, Si, V, Cr, Mn, Fe, Co, Ni, Cu, Zn, Mo, Sn, and W. In contrast, elements that occupy the A-site comprise a smaller list: Ti [1], Zr, Hf [2–4], Nb

[4–6], and Y [6]. Among these A-site elements, Y is the least understood modifier for Zr-based AB₂ MH alloys.

Y immediately precedes Zr in the periodic table. Due to its relatively large atomic radius and small electronegativity, Y is expected to occupy the A-site in Laves phase alloys. A few Y-based C15 alloys, such as YMn₂ [7–9], YFe₂ [10–12], YCo₂ [13], and YNi₂ [12,14–16], showed significant amounts of gaseous phase hydrogen storage but have not been modified with substitution elements for the purpose of adjusting the performance characteristics to be suitable for electrochemical applications. Results of previous investigations of the electrochemical influence of Y as a modifier in some alloy systems are summarized in the remainder of this paragraph. As a partial substitution of Zr in a C14 AB₂ alloy, Y enlarged the unit cell, decreased the electrochemical capacity, and facilitated activation [6]. In C14/BCC-mixed AB₂ alloys, replacing a small amount of Ti with Y improved the electrochemical capacity,

* Corresponding author. Tel.: +1 248 293 7000; fax: +1 248 299 4520.

E-mail addresses: kwyoung@yahoo.com, kyoung@ovonic.com (K. Young).

cycle stability, and high-rate dischargeability (HRD) [17,18]. In AB₅ alloys, while adding Y to the alloy formula increased the pulverization rate during hydride/dehydride cycling [19] and improved high temperature performance [20], adding Y₂O₃ powder to the electrode reduced the surface corrosion and improved the cycle stability [21]. In Mg₂Ni MH alloys prepared by mechanical alloying, the addition of Y increased the capacity [22], HRD [23], surface exchange current [22], and cycle stability [23]. Since no report on examining Y-substitution in C14/C15 multi-phase AB₂ alloys was available in the literature, the current study was deemed necessary and therefore conducted.

2. Experimental setup

Arc melting was performed under a continuous argon flow with a non-consumable tungsten electrode and a water-cooled copper tray. Before each run, a piece of sacrificial titanium underwent a few melting–cooling cycles to reduce the residual oxygen concentration. Each 12-g ingot was re-melted and turned over repeatedly to ensure uniformity in chemical composition. The chemical composition of each sample was examined by a Varian Liberty 100 inductively-coupled plasma (ICP) system. A Philips X'Pert Pro X-ray diffractometer (XRD) was used to study the microstructure, and a JEOL-JSM6320F scanning electron microscopy (SEM) with energy dispersive spectroscopy (EDS) capability was used to study the phase distribution and composition. The gaseous phase hydrogen storage characteristics for each sample were studied by pressure–concentration–temperature (PCT) isotherm measurement using a Suzuki-Shokan multi-channel PCT system. In the PCT analysis, each sample was first activated by a 2-h thermal cycle between 300 °C and room-temperature at 25 atm H₂ pressure. The PCT isotherms at 30 and 60 °C were then measured. Details of both electrode and cell preparations as well as measurement methods have been previously reported [24,25].

3. Results and discussion

Two series of alloys (177-Ti₁₂Zr_{21.5–x}Y_xV₁₀Cr_{8.5}Mn_{5.6}Co_{1.5}Ni_{40.2}Sn_{0.3}Al_{0.4} and 193-Ti₁₂Zr_{21.5–x}Y_xV₁₀Cr_{3.5}Mn_{4.1}Co_{8.0}Ni_{40.2}Sn_{0.3}Al_{0.4}, $x = 0–4$) were designed with partial substitution of Zr by Y. The base alloys (177 and 193) for these two series were chosen based on earlier studies of C14/C15-mixed structures [26–28] and

influences from phase abundance [29] and stoichiometry [30,31]. The designed composition, average electron density (e/a), and B/A stoichiometric ratio for each alloy are listed in Table 1. According to the designed compositions, the two series of alloys were stoichiometric AB₂ alloys with the dominating phase being C14 for the 177-series and the dominating phase being C15 for the 193-series due to the difference in number of outer-shell electrons between Cr and Co (six and nine, respectively) [32,33]. The ICP results, shown in the same table, were close to the designed values except for small Mn-inhomogeneities present in the arc-melted samples. The calculated e/a values and B/A ratios based on the average alloy compositions from ICP analysis were very close to the designed values.

3.1. XRD structure analysis

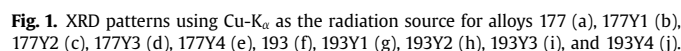
The XRD patterns of the 10 alloys are displayed in Fig. 1. All the major peaks could be fit into hexagonal C14 (MgZn₂) and face-center-cubic C15 (MgCu₂) structures with many overlaps. Besides the Laves phases, minor phases, such as TiNi, Zr₇Ni₁₀, YNi, and Y₂O₃, were also present. The lattice constants, a/c aspect ratio, and unit cell volumes of the C14 and C15 phases calculated from the XRD pattern for each alloy are listed in Table 2. As the Y-content increased in both series of alloys, the lattice constants a and c , and the unit cell volumes of both C14 and C15 phases decreased. Y, with its larger metallic radius in the Laves phase alloy (1.990 Å) compared to the replaced Zr (1.771 Å) [34], was expected to increase the lattice constants and unit cell volume (assuming that the distribution of Y was uniform throughout the alloy). This finding of unit cell shrinkage with Y-addition (as shown in Fig. 2) will be further discussed in the SEM/EDS section.

The C14 and C15 crystallite sizes of each alloy were estimated by the Scherrer equation [35] using the full-width at half maximum of the C14 (103) and C15 (220) peaks in the XRD pattern and are listed in Table 2. The Y-containing alloys in the 177-series had smaller C14 and larger C15 crystallites compared to the base alloy while the trends of the changes in crystallite sizes in the 193-series were not clear.

The phase abundances analyzed by Jade 9 software are listed in Table 2. In both series, the addition of Y increased the C15 phase abundance. The microstructure of the 177-series changed from being C14-predominant to a mixture of C14:C15 = 2:3 while that of the 193-series remained C15-predominant with Y-addition. The

Table 1
Designed compositions and ICP results in at.%.

Alloy number		Ti	Zr	V	Cr	Mn	Co	Ni	Sn	Al	Y	e/a	B/A
177	Design	12.0	21.5	10.0	8.5	5.6	1.5	40.2	0.3	0.4	0.0	6.951	1.99
	ICP	12.2	21.6	10.2	8.4	4.8	1.5	40.6	0.3	0.5	0.0	6.954	1.96
177Y1	Design	12.0	20.5	10.0	8.5	5.6	1.5	40.2	0.3	0.4	1.0	6.941	1.99
	ICP	12.2	20.5	10.0	8.4	5.2	1.5	40.4	0.3	0.4	1.0	6.935	1.96
177Y2	Design	12.0	19.5	10.0	8.5	5.6	1.5	40.2	0.3	0.4	2.0	6.931	1.99
	ICP	12.4	19.8	10.0	8.2	4.8	1.5	40.5	0.4	0.5	1.9	6.929	1.93
177Y3	Design	12.0	18.5	10.0	8.5	5.6	1.5	40.2	0.3	0.4	3.0	6.921	1.99
	ICP	12.4	18.5	10.1	8.3	4.1	1.5	41.2	0.3	0.6	2.9	6.928	1.96
177Y4	Design	12.0	17.5	10.0	8.5	5.6	1.5	40.2	0.3	0.4	4.0	6.911	1.99
	ICP	12.3	17.6	10.2	8.5	4.4	1.5	40.9	0.4	0.5	3.8	6.934	1.97
193	Design	12.0	21.5	10.0	3.5	4.1	8.0	40.2	0.3	0.4	0.0	7.131	1.99
	ICP	12.0	21.4	10.1	3.6	3.5	8.1	40.5	0.4	0.4	0.0	7.149	1.99
193Y1	Design	12.0	20.5	10.0	3.5	4.1	8.0	40.2	0.3	0.4	1.0	7.121	1.99
	ICP	11.9	20.4	10.2	3.6	3.7	8.1	40.3	0.3	0.3	1.1	7.120	1.99
193Y2	Design	12.0	19.5	10.0	3.5	4.1	8.0	40.2	0.3	0.4	2.0	7.111	1.99
	ICP	12.0	19.2	10.0	3.5	3.5	8.0	40.8	0.3	0.5	2.2	7.126	1.99
193Y3	Design	12.0	18.5	10.0	3.5	4.1	8.0	40.2	0.3	0.4	3.0	7.101	1.99
	ICP	12.2	18.5	10.0	3.5	3.4	8.0	40.7	0.4	0.5	2.9	7.124	1.98
193Y4	Design	12.0	17.5	10.0	3.5	4.1	8.0	40.2	0.3	0.4	4.0	7.091	1.99
	ICP	12.1	17.6	10.1	3.5	3.0	8.0	41.0	0.3	0.6	3.7	7.104	1.99



3.2. SEM/EDS analysis

The Y-content in the AB₂ main phase was only 10–20% of the overall Y-content for each Y-substituted alloy. Y is preferred to stay in the (Y, Sn)-rich and Y₂O₃ secondary phases rather than become incorporated into the main AB₂ phase. According to the crystal structures of YX₂ inter-metallic compounds shown in Table 4, Y forms Laves phase with many transition metals. Since the evolution of the formed phase is strongly related to the total

Table 2
Summary of XRD and gaseous phase storage properties of alloys in this study.

Alloy number	C14 lattice constant <i>a</i> (Å)	C14 lattice constant <i>c</i> (Å)	<i>a/c</i> aspect ratio	C14			C15			C14 phase abundance (%)	C15 phase abundance (%)	Zr ₇ Ni ₁₀ phase abundance (%)	TiNi phase abundance (%)	YNi phase abundance (%)	Y ₂ O ₃ phase abundance (%)
				C14 unit cell volume, (Å ³)	C14 crystallite size (Å)	C15 lattice constant <i>a</i> (Å)	C15 unit cell volume (Å ³)	C15 crystallite size (Å)							
177	4.977	8.138	0.6115	174.6	638	7.017	345.6	407	74	11	ND	15	ND	ND	ND
177Y1	4.970	8.110	0.6128	173.5	503	7.012	344.8	505	40	60	ND	ND	ND	ND	0.6
177Y2	4.970	8.113	0.6126	173.5	514	7.013	344.9	453	37	56	4	ND	3	ND	ND
177Y3	4.966	8.121	0.6116	173.4	430	7.011	344.7	470	41	54	2	ND	3	ND	ND
177Y4	4.963	8.104	0.6124	172.8	479	7.008	344.2	458	40	54	1	ND	4	0.7	ND
193	4.978	8.112	0.6137	174.1	872	7.003	343.4	647	32	67	ND	1	ND	ND	ND
193Y1	4.961	8.088	0.6133	172.4	>1000	6.998	342.7	595	13	84	ND	3	ND	ND	ND
193Y2	4.956	8.092	0.6124	172.1	>1000	6.994	342.1	646	17	83	ND	ND	ND	ND	0.6
193Y3	4.954	8.069	0.6140	171.5	859	6.989	341.4	736	11	89	ND	ND	ND	ND	ND
193Y4	4.952	8.073	0.6134	171.5	667	6.987	341.0	672	18	79	ND	ND	2	0.5	ND

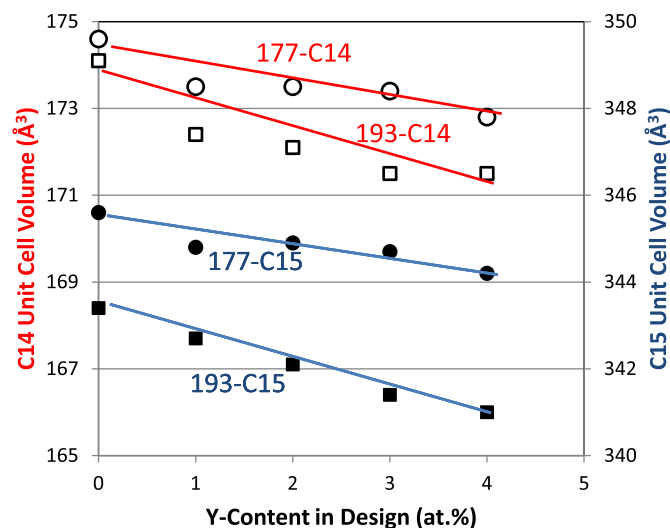


Fig. 2. C14 and C15 unit cell volumes of 177- and 193-series of alloys as functions of average Y-content in design.

number of outer-shell electrons per AB_2 formula (3 times e/a) [39], the similarity between Table 4 (structures of YX_2) and Table 5 (structures of ZrX_2) was not surprising because Zr has one more outer-shell electron than Y does. The original design concept was to dope the alloy with Y in order to stabilize the Laves phase (Ni is a major B-site element, but there is no inter-metallic compound between Zr and Ni). However, the EDS results have shown a very limited solubility of Y in the (Zr, Ti)-based main AB_2 phase, which was consistent with the immiscibility between Y and both Zr and Ti as can be seen from the corresponding binary phase diagrams [36].

Only after annealing can Y be fully incorporated into Laves phase ($ZrFe_2$ [40]) and non-Laves phase alloys ($ZrCo_{2.9}$ [41] and $ZrNiSn$ [42,43]). The reduction in amount of the relatively large-sized Zr in the main AB_2 phase was the main reason for both the unit cell shrinkages in C14 and C15 shown in Fig. 2 and the increase in B/A ratio. While the main phases in the base alloys were either stoichiometric (177) or hypo-stoichiometric (193), the main phases in most of the Y-doped alloys were hyper-stoichiometric. The importance of stoichiometry to the electrochemical properties of multi-phase AB_2 MH alloys has been reported [30,44]; hyper-stoichiometry with B/A ratio of 2:1 promotes C15 and shows the best electrochemical HRD.

Besides the main AB_2 phase (which contained a very small amount of Y), there was another AB_2 phase (denoted as AB_2 -2 in Table 3 and seen as Fig. 3b-4 and d-1) with higher Y-content and relatively low V- and Cr-contents found in alloys with designed Y-levels higher than 1 at.%. According to its e/a ratio, this phase should have a C15 structure. In the non-Laves secondary phases, the one showing the brightest contrast was very rich in both Sn and Y (denoted as (Y, Sn)-rich and seen as Fig. 3a-1, b-1 and d-1). The phases with the closest compositions found from the phase diagram are $Y_{11}Sn_9$ and Y_5Sn_4 [45]. However, the corresponding XRD peaks were difficult to be identified due to low abundance and severely overlapping with peaks from Laves phases. An alloy with the same composition as the Fig. 3b-1 phase prepared by arc melting showed 43% $Y_{11}Sn_9$, 25% $YNiSn$, 15% Sn, 9% Y_2Sn_5 and 7% YSn_2 ; therefore, the (Y, Sn)-rich phase is most likely dominated by $Y_{11}Sn_9$. This alloy showed no hydrogen storage capability according to the PCT analysis. The same alloy showed strong reactivity with water due to its high Y-content and dissolved completely in 30 wt.% KOH solution. The AB phase could be either TiNi (in the Y-free alloys) or YNi (in the alloys with 3 and 4 at.% Y and can be seen as Fig. 3b-2, b-3 and d-3). Both TiNi and YNi are hydride formers. PCT

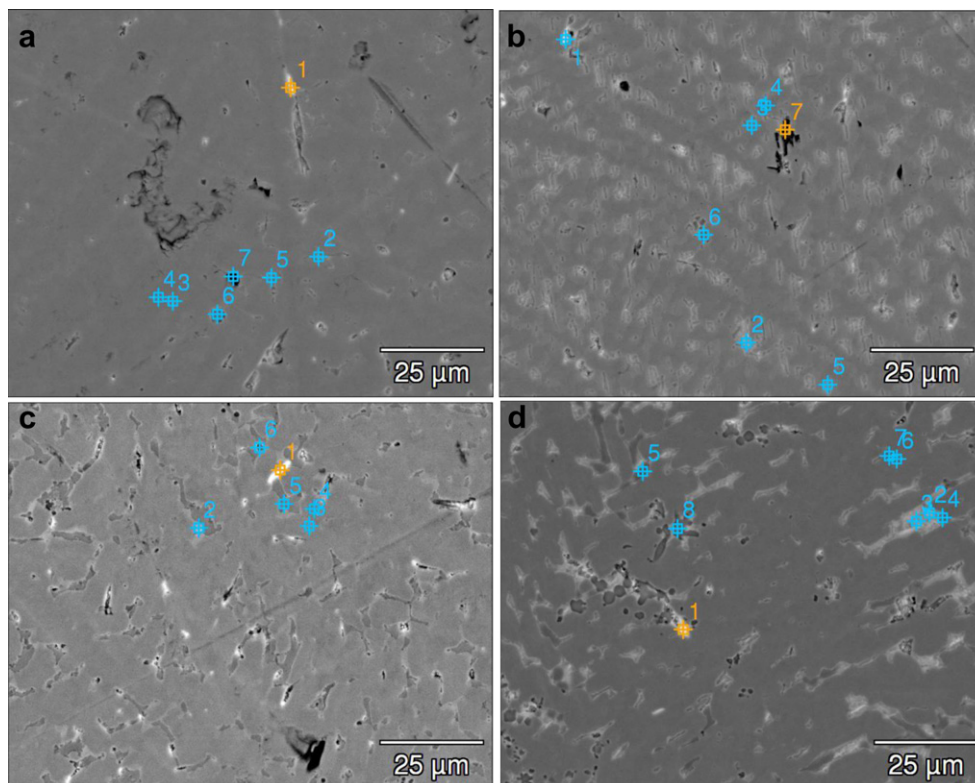


Fig. 3. SEM back-scattering electron images for alloys 177Y1 (a), 177Y4 (b), 193Y1 (c), and 193Y4 (d).

Table 3EDS results in at.% from areas identified in SEM micrographs (Fig. 3). Compositions of main AB₂ phases are highlighted in bold.

Alloy number	Area	Ti	Zr	V	Cr	Mn	Co	Ni	Sn	Al	Y	B/A	e/a	Phase
177Y1	Fig. 3a-1	9.5	11.8	4.1	2.9	2.2	0.9	32.0	15.1	0.8	20.5	1.4	7.42	Y, Sn-rich
	Fig. 3a-2	11.9	20.8	11.0	8.7	4.8	1.6	40.2	0.2	0.5	0.3	2.0	6.93	AB ₂
	Fig. 3a-3	9.5	21.4	13.4	14.6	6.1	1.9	32.5	0.1	0.5	0.1	2.2	6.66	AB₂
	Fig. 3a-4	11.4	20.7	11.7	9.4	5.4	1.7	39.0	0.2	0.5	0.1	2.1	6.91	AB ₂
	Fig. 3a-5	12.7	20.9	8.9	6.2	4.4	1.3	44.6	0.1	0.5	0.3	1.9	7.08	AB ₂
	Fig. 3a-6	11.0	20.8	12.2	10.9	5.5	1.8	37.1	0.1	0.6	0.1	2.1	6.83	AB ₂
	Fig. 3a-7	13.5	20.7	8.2	5.8	4.1	1.4	45.5	0.0	0.5	0.3	1.9	7.11	AB ₂
177Y4	Fig. 3b-1	4.0	5.5	2.0	1.6	1.0	0.5	14.2	35.4	0.4	35.3	1.2	8.14	Y, Sn-rich
	Fig. 3b-2	6.0	8.7	2.3	1.7	1.4	0.5	53.2	0.5	0.7	24.5	1.5	7.09	AB
	Fig. 3b-3	9.7	12.7	4.4	3.5	2.4	0.8	50.4	0.2	0.9	15.1	1.7	7.11	AB
	Fig. 3b-4	11.4	17.5	9.0	7.4	4.0	1.4	44.4	0.1	0.7	4.0	2.0	7.05	AB ₂ -2
	Fig. 3b-5	13.0	18.7	11.5	8.8	4.4	1.6	40.8	0.0	0.5	0.6	2.1	6.94	AB₂
	Fig. 3b-6	11.3	12.1	6.1	4.5	3.2	1.1	36.2	0.0	0.4	25.2	1.1	6.22	Y ₂ O ₃
	Fig. 3b-7	10.9	7.3	2.7	1.9	1.6	0.4	61.1	0.3	0.7	13.1	2.2	7.69	Y ₂ O ₃
193Y1	Fig. 3c-1	18.6	15.4	3.2	0.8	1.6	4.4	46.3	2.3	0.5	6.9	1.4	7.25	Zr ₇ Ni ₁₀
	Fig. 3c-2	24.1	17.1	2.1	0.5	1.3	5.0	48.6	0.0	0.5	0.7	1.4	7.22	Zr ₇ Ni ₁₀
	Fig. 3c-3	10.5	21.1	12.5	4.5	3.9	9.3	37.4	0.2	0.4	0.1	2.2	7.05	AB₂
	Fig. 3c-4	11.7	21.0	10.2	3.3	3.3	8.2	41.1	0.1	0.5	0.3	2.0	7.13	AB ₂
	Fig. 3c-5	21.6	17.0	2.8	0.6	1.5	4.9	48.9	0.3	0.5	1.7	1.5	7.26	Zr ₇ Ni ₁₀
	Fig. 3c-6	20.1	12.1	2.4	0.5	1.3	4.1	38.7	16.9	0.4	3.4	1.8	8.25	SnO ₂
	Fig. 3d-1	11.0	17.7	6.1	1.6	2.6	5.4	48.6	0.6	0.8	5.6	1.9	7.35	AB ₂ -2
193Y4	Fig. 3d-2	9.5	14.4	3.6	1.0	2.3	3.3	54.3	0.1	1.1	10.6	1.9	7.45	AB ₂ -2
	Fig. 3d-3	5.5	8.7	2.3	0.7	1.5	2.3	52.5	0.2	0.9	25.3	1.5	7.10	AB
	Fig. 3d-4	12.4	19.0	10.2	3.3	2.8	8.3	42.3	0.0	0.6	1.1	2.1	7.19	AB ₂
	Fig. 3d-5	25.6	11.1	1.4	0.2	1.3	4.5	49.1	0.1	0.9	5.7	1.4	7.17	AB/AB ₂
	Fig. 3d-6	11.6	19.7	11.4	3.6	3.2	9.0	40.3	0.0	0.5	0.6	2.1	7.14	AB ₂
	Fig. 3d-7	12.7	18.9	10.7	3.3	3.1	8.5	41.5	0.0	0.6	0.7	2.1	7.17	AB₂
	Fig. 3d-8	5.8	6.2	2.7	1.0	1.2	2.3	25.4	0.1	0.8	54.6	0.5	5.18	Y ₂ O ₃

analysis of an YNi alloy prepared by arc melting showed a maximum and a reversible hydrogen storage capacity of 0.85 and 0.45 wt.%, respectively. Occasionally, metal oxide inclusions, such as ZrO₂, SnO₂ (Fig. 3c-6), and Y₂O₃ (Fig. 3b-6, 3b-7, and 3d-8), were also found in the alloys.

3.3. Gaseous phase study

The gaseous phase hydrogen storage properties of the alloys were studied by 30 and 60 °C PCT measurements. The resulting absorption and desorption isotherms measured at 30 °C are displayed in Fig. 5. The information obtained from the PCT study is summarized in Table 5. Due to the high plateau pressures of these two series of alloys, only the 30 °C PCT isotherms of the 177-series showed complete α (metal)-to- β (hydride) transitions while the end-points of the plateau regions in the other three sets of isotherms were above the available maximum hydrogen pressure of the PCT apparatus (1.12 MPa). In the 177-series, both the maximum and reversible hydrogen storage capacities decreased as the Y-content increased. These decreases were due to the unit cell shrinkage found in XRD (Fig. 3) that can be attributed to the decreasing Zr-content in the main phase as the Y-content increased (Fig. 4a). In the 193-series, both the maximum and the reversible hydrogen storage capacities measured at 30 °C increased and later decreased as the Y-content increased. This finding differed from what was predicted by the unit cell shrinkage but can be explained by the incomplete PCT isotherm caused by the high plateau pressure. For the same reason, the increase in hydrogen storage capacity with increasing Y-content was not observed in the 60 °C isotherms (Fig. 5d). For both series, the 30 °C mid-points of the desorption isotherms of the Y-doped alloys were lower than that of the Y-free base alloy. This finding was interesting because the smaller unit cells found in the Y-doped alloys have usually been associated with less stable hydrides with higher plateau pressures [46,47]. Intersections in a series of PCT isotherms, as seen in Fig. 5a, with one controlling factor have seldom been seen. In addition, calculations

of the heat of hydride formation for the alloys (based on the atomic percentages and corresponding heats of hydride formation of the constituent elements [48,49] in the main phase) showed that the Y-doped alloys had higher (less negative value) heats of hydride formation than the Y-free base alloy did in both series, which supported the argument that the metal-hydrogen bond strength decreases with the addition of Y.

The hysteresis of the PCT isotherm, listed in Table 6, has conventionally been defined as $\ln(P_a/P_d)$, where P_a and P_d are the absorption and desorption mid-point pressures, respectively. The amount of hysteresis is positively correlated with (and thus can be used to predict) the pulverization rate of the alloy during cycling [50–52]. In the current study, the Y-doped alloys had slightly larger hysteresis; therefore, higher pulverization rates during hydride/dehydride cycling were expected with the addition of Y.

The slope factor has conventionally been defined as the ratio of the storage capacity between 0.01 and 0.5 MPa to the maximum capacity and can be related to the degree of disorder in the alloy [53,54]. In the current study, the slope factor value did not change by much with Y-addition since only a small amount of Y was incorporated into the main phase, which suggested that Y-addition did not change the degree of disorder in the alloy.

3.4. Electrochemical measurement

The discharge capacity of each alloy was measured in a flooded-cell configuration against a partially pre-charged Ni(OH)₂ positive electrode. No alkaline pretreatment was applied before the half-cell measurement. Each sample electrode was charged at a constant current density of 50 mA g⁻¹ for 10 h and then discharged at a current density of 50 mA g⁻¹ followed by two pulls at 12 and 4 mA g⁻¹. The obtained full capacities (4 mA g⁻¹) from the first 13 cycles are plotted in Fig. 6a and b for the 177- and 193-series of alloys, respectively. While the Y-free base alloys needed one or two cycles to reach the stabilized full capacities, almost all of the Y-doped alloys reached the same status in the first cycle,

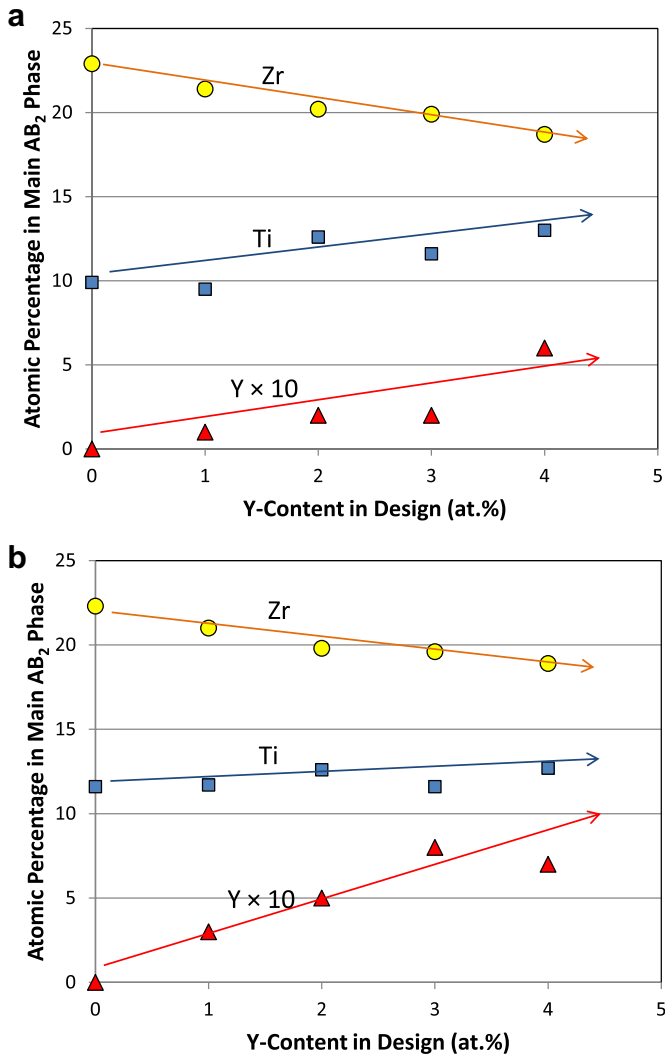


Fig. 4. The Zr, Ti, and Y-contents in the main AB₂ phase as functions of average Y-content for 177- (a) and 193-series of alloys (b).

demonstrating a faster activation. In the 177-series, the full capacity decreased with the increase in Y-content, which was consistent with the decrease in gaseous phase hydrogen storage capacity found from PCT measurements and the shrinking unit cell volume found in XRD analysis. In the 193-series, the full capacities of the Y-containing alloys were similar and lower than that of the Y-free base alloy. This finding was consistent with the XRD result (smaller unit cell with Y-addition), but it was different from the trend observed in gaseous phase hydrogen storage capacity measured at 30 °C. HRD values, defined as the ratio of capacities measured at

Table 4
List of atomic numbers of X and crystal structures of inter-metallic compounds YX₂ (data from Refs. [36–38]).

23	24	25	26	27	28	29	30
V	Cr	Mn	Fe	Co	Ni	Cu	Zn
Immiscible	Immiscible	C15	C15	C15	C15	CeCu ₂	CeCu ₂
41	42	43	44	45	46	47	48
Nb	Mo	Tc	Ru	Rh	Pd	Ag	Cd
Immiscible	Immiscible	C14	C14	C15	No IMC	C11 _b	C6
73	74	75	76	77	78	79	80
Ta	W	Re	Os	Ir	Pt	Au	Hg
Immiscible	Immiscible	C14	C14	C15	C15	C11 _b	C32

Table 5
List of atomic numbers of X and crystal structure of inter-metallic compounds ZrX₂ (data from Refs. [36,37]).

23	24	25	26	27	28	29	30
V	Cr	Mn	Fe	Co	Ni	Cu	Zn
C15	C14	C14	C15	C15	No IMC	No IMC	C15
41	42	43	44	45	46	47	48
Nb	Mo	Tc	Ru	Rh	Pd	Ag	Cd
Immiscible	C15	C14	C14	No IMC	C11 _b	No IMC	C15
73	74	75	76	77	78	79	80
Ta	W	Re	Os	Ir	Pt	Au	Hg
Immiscible	C15	C14	C14	C15	No IMC	C11 _b	No IMC

discharge current densities of 50 mA g⁻¹ and 4 mA g⁻¹, for the first 13 cycles are plotted in Fig. 6c and d for 177- and 193-series of alloys, respectively. In both series of alloys, as the Y-content in the alloy increased, the HRD values stabilized more quickly and

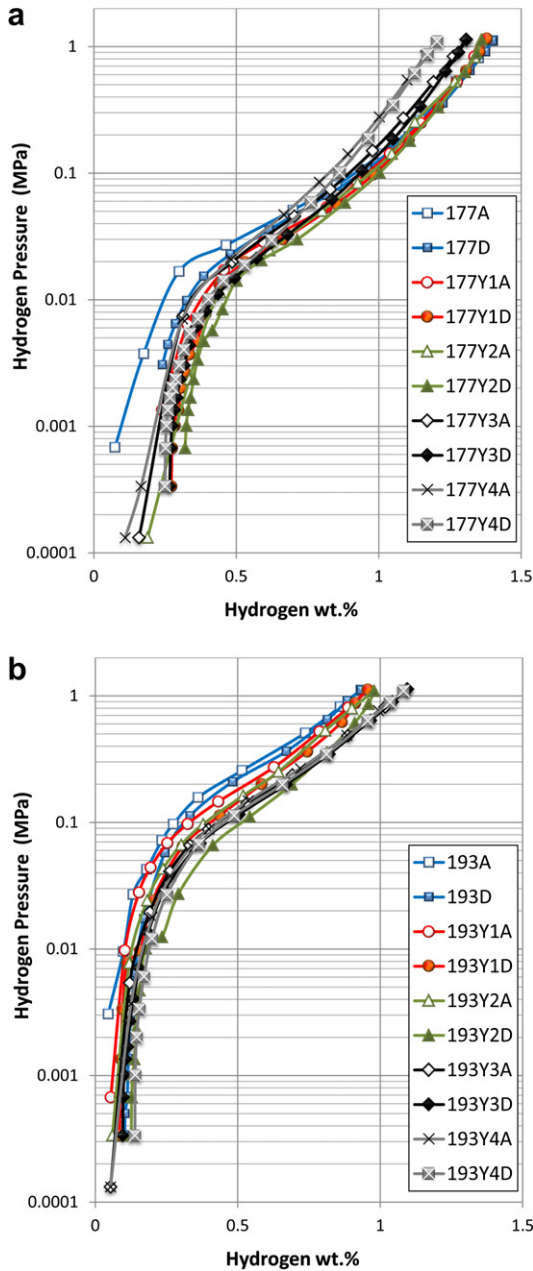


Fig. 5. PCT isotherms of 177- (a) and 193-series of alloys (b) measured at 30 °C. Open and solid symbols are for absorption and desorption curves, respectively.

Table 6

Summary of gaseous phase hydrogen storage properties of alloys in this study.

Alloy number	Max. H-storage at 30 °C (wt.%)	Max. H-storage at 60 °C (wt.%)	Rev. H-storage at 30 °C (wt.%)	Mid-point pressure at 30 °C desorption (MPa)	30 °C PCT hysteresis	30 °C PCT slope factor
177	1.40	1.21	1.16	0.066	0.11	0.79
177Y1	1.38	1.32	1.11	0.054	0.17	0.77
177Y2	1.36	1.27	1.04	0.051	0.16	0.77
177Y3	1.31	1.28	1.04	0.053	0.20	0.75
177Y4	1.20	1.15	0.95	0.051	0.24	0.73
193	0.93	0.93	0.83	0.24	0.07	0.74
193Y1	0.96	0.90	0.88	0.16	0.34 ^a	0.69
193Y2	0.98	0.85	0.85	0.12	0.46 ^a	0.70
193Y3	1.10	0.87	1.00	0.16	0.11	0.66
193Y4	1.08	0.86	0.94	0.18	0.11	0.65

^a Denotes large hysteresis due to the presence of dual phases.

reached a higher value. The full capacity and the HRD value of each alloy at cycle 10 are listed in Table 7. In the 177-series, the HRD value increased with the increase in Y-content alloys due to the catalytic contribution from the Y-containing secondary phases and also the increase in C15 phase which is known for better HRD [29]. In the 193-series, the HRD value increased more dramatically with the increase in Y-content for the same reason as in the 177-series. The cycle number at which HRD reaches 90% can be used to evaluate the activation behavior and is listed in Table 7 for each alloy. In both series, the number of activation cycles decreased with the increase in Y-content. Both the Y-containing secondary phases and the increase in C15-abundance [55] contributed to an easier activation. To summarize the electrochemical results obtained thus far, the partial substitution of Zr by Y facilitated activation and increased HRD but reduced the full capacity in both series of alloys.

In order to further understand the source of the increase in HRD with the increase in Y-content, both the bulk diffusion coefficient and the surface exchange current were measured. The details of both parameters' measurements have been reported previously [56], and the values are listed in Table 7. In the 177-series, the increase in HRD was mainly due to the better bulk diffusion from the higher C15 phase abundance. The C15 phase was found to carry a higher bulk diffusion rate than the C14 phase does, as reported in a previous study of AB₂ alloys [29]. In the 193-series, the increase in HRD came from the combination of increased bulk diffusion and surface reaction, which is similar to the case of Mo-modified AB₂ alloys [57].

The low-temperature characteristics were studied with an AC impedance measurement conducted at –40 °C. Pressed electrodes were activated in 30 wt.% KOH solution at 100 °C for 4 h before the

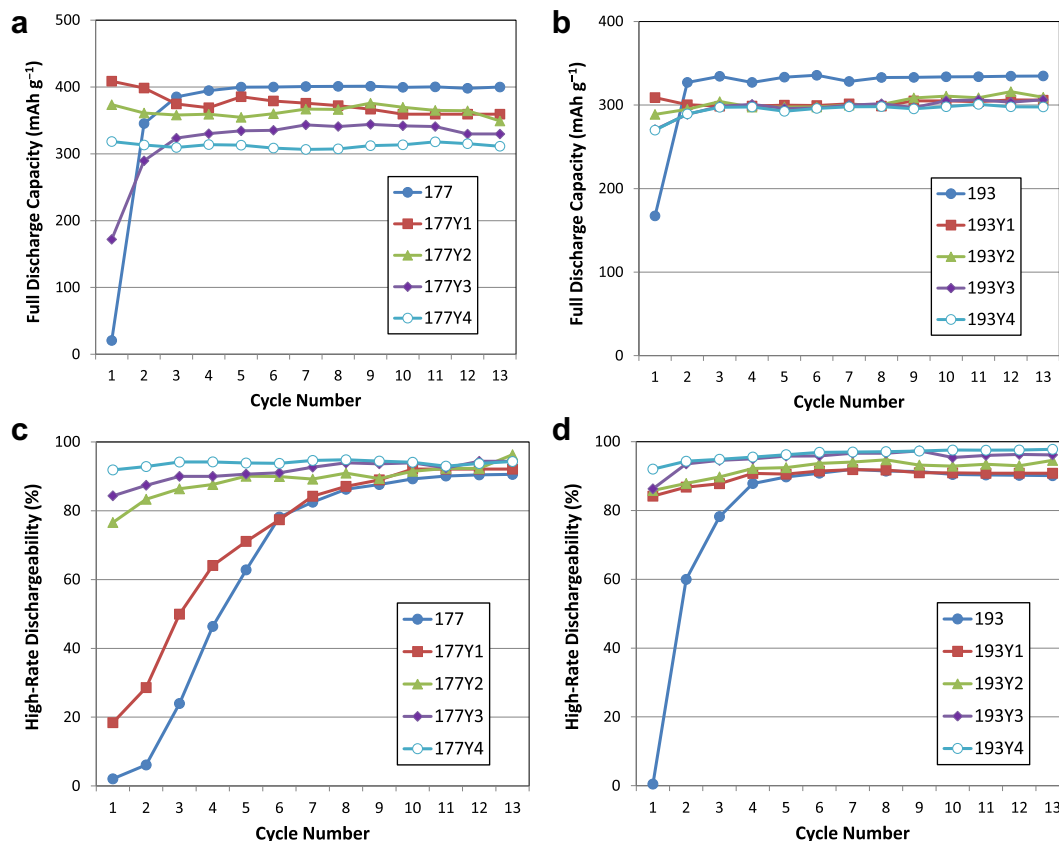
**Fig. 6.** The half-cell discharge capacity of at 4 mA g⁻¹ for 177- (a) and 193-series (b), and full HRD for 177- (c) and 193-series (d) of the first 13 cycles.

Table 7
Summary of electrochemical properties of alloys in this study.

Alloy number	Full capacity @ 10th cycle (mAh g ⁻¹)	High-rate dischargeability @ 10th cycle	Cycle number reaches 90% HRD	Diffusion coefficient (×10 ⁻¹¹ cm ² s ⁻¹)	Exchange current (mA g ⁻¹)	Charge transfer resistance @ -40 °C (Ω g)	Double-layer capacitance @ -40 °C (F g ⁻¹)	RC product @ -40 °C (s)
177	399	89%	11	5.6	25.8	184	0.12	22.1
177Y1	359	92%	10	10.8	5.6	261	0.29	75.7
177Y2	370	91%	8	12.4	19.1	97	0.40	38.8
177Y3	342	94%	5	12.4	19.3	44	0.43	18.9
177Y4	313	94%	1	12.5	16.3	42	0.56	23.5
193	335	90%	6	12.1	26.3	128	0.17	21.8
193Y1	305	91%	4	12.8	24.5	97	0.20	19.4
193Y2	310	93%	4	33.5	31.8	74	0.18	13.3
193Y3	305	95%	2	31.9	41.6	49	0.27	13.2
193Y4	298	98%	1	54.4	36.3	23	0.66	15.2

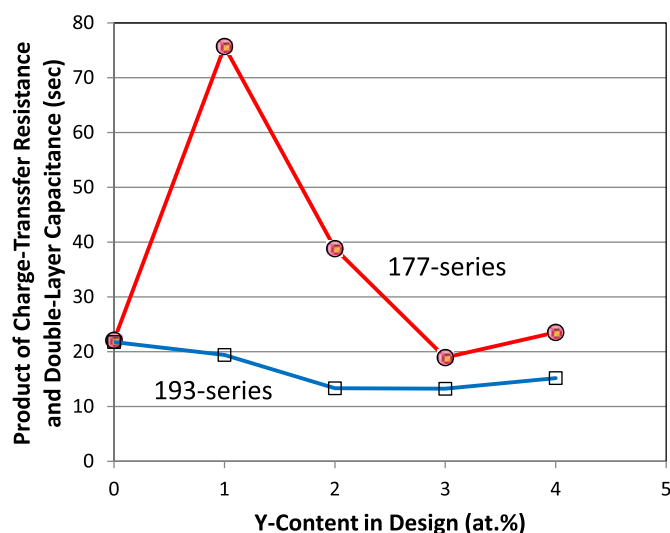


Fig. 7. The product of charge transfer resistance and double-layer capacitance measured at -40 °C as a function of average Y-content.

measurement. The charge transfer resistance (R), double-layer capacitance (C), and the RC product of each alloy were calculated from the Cole–Cole plot and are listed in Table 7. In the 177-series, as the Y-content increased, the -40 °C resistance decreased (except for alloy 177Y1, which also showed a low room-temperature exchange current) due to the increased surface area as seen from the increase in double-layer capacitance. The RC product (which excludes the contribution from the surface area and has been used previously in other MH alloy works [57–59]) is plotted in Fig. 7 as a function of the designed Y-content. The curve showed a large increase in the beginning and a decrease afterward as the Y-content increased. The -40 °C electrochemical performance of the 177-series were benefited mainly from the increase in surface area. In the 193-series, the increase in surface area was not as prominent with the exception of 193Y4. Judging from the RC plot in Fig. 7, the decrease in -40 °C charge transfer resistance was not due to the increase in surface area but rather was due to the more reactive surface. The Y-containing secondary phases play a crucial role in improving activation, HRD, and low-temperature performance.

4. Summary

Two series of alloys (177-Ti₁₂Zr_{21.5-x}Y_xV₁₀Cr_{8.5}Mn_{5.6}Co_{1.5}Ni_{40.2}Sn_{0.3}Al_{0.4} and 193-Ti₁₂Zr_{21.5-x}Y_xV₁₀Cr_{3.5}Mn_{4.1}Co_{8.0}Ni_{40.2}Sn_{0.3}Al_{0.4}, $x = 0-4$) were prepared by arc melting. While the base alloy in the first series has a C14-dominated microstructure, the base

alloy in the second series is dominated by C15 phase. In both series, most of the added Y went into the non-Laves minor phases. As a result, although Y is larger than the replaced Zr, the unit cell volumes of both C14 and C15 main Laves phases decreased as the Y-content in the alloy increased, which caused reductions in both gaseous phase hydrogen storage and electrochemical. The addition of Y increased the C15 phase abundance due to its effect in shifting the main phase from stoichiometric or hypo-stoichiometric to hyper-stoichiometric. Y-incorporation also promoted the formation of (Y, Sn)-rich secondary phases having high solubility in KOH electrolyte. Both C15 and (Y, Sn)-rich phases contributed to the improvements in activation and high-rate dischargeability. During the study of source of the improved HRD, we found bulk diffusion alone is the key contributor in 177-series, and both bulk and surface reaction are important for 193-series of alloys. Besides, AC impedance measured at -40 °C showed substantial reduction in surface charge transfer resistance in both series. While the surface area measured at -40 °C increased with the increasing Y-content in the 177-series and thereby reduced the charge transfer resistance, the surface area in the 193-series did not deviate from the base alloy's level (except for 193Y4), indicating that the increase in surface reactivity brought on by the contributions from the secondary phases was the main reason of the reduction in charge transfer resistance.

References

- [1] K. Young, M.A. Fetcenko, F. Li, T. Ouchi, J. Alloys Compd. 464 (2008) 238.
- [2] Ewa Rönnebro, Dag Noréus, Makoto Tsukahara, Tetsuo Sakai, J. Alloys Compd. 293–295 (1999) 169.
- [3] H.T. Takeshita, N. Fujiwara, N. Takeichi, H. Senoh, T. Oishi, J. Alloys Compd. 404–406 (2005) 609.
- [4] J. Huot, E. Akiba, T. Ogura, Y. Ishido, J. Alloys Compd. 218 (1995) 101.
- [5] H. Nakano, S. Wakao, J. Alloys Compd. 231 (1995) 587.
- [6] A.R. dos Santos, R.C. Ambrosio, E.A. Ticianelli, Int. J. Hydrogen Energy 29 (2004) 1253.
- [7] H. Fujii, M. Saga, T. Okamoto, J. Less Common Met. 130 (1987) 25.
- [8] J. Przewoznik, V. Paul-Boncour, M. Latroche, A. Percheron-Guégan, J. Alloys Compd. 225 (1995) 436.
- [9] M. Latroche, V. Paul-Boncour, J. Przewoznik, A. Percheron-Guégan, F. Bourée-Vigneron, J. Alloys Compd. 231 (1995) 99.
- [10] T. Okamoto, H. Fujii, S. Takeda, T. Hihara, J. Less Common Met. 88 (1982) 181.
- [11] H. Fujii, T. Okamoto, W.E. Wallace, F. Pourarian, T. Morisaki, J. Magn. Mater. 46 (1985) 245.
- [12] K. Suzuki, X. Lin, J. Alloys Compd. 193 (1993) 7.
- [13] K. Fujiwara, K. Ichinose, H. Nagai, A. Tsujimura, J. Magn. Mater. 90–91 (1990) 561.
- [14] S. Orimo, H. Fujii, M. Tabata, J. Alloys Compd. 210 (1994) 37.
- [15] K. Funaki, S. Orimo, H. Fujii, J. Alloys Compd. 253–254 (1997) 110.
- [16] M. Nakhl, B. Chevalier, J.-L. Bobert, B. Darriet, J. Alloys Compd. 314 (2001) 275.
- [17] H. Miao, M. Gao, Y. Liu, Y. Lin, J. Wang, H. Pan, J. Electrochem. Soc. 154 (2007) A1010.
- [18] M. Gao, H. Miao, Y. Zhao, Y. Liu, H. Pan, J. Alloys Compd. 484 (2009) 249.
- [19] O. Arnaud, P. Barbic, P. Bernard, A. Bouvier, B. Knosp, B. Riegel, M. Wohlfahrt-Mehrens, J. Alloys Compd. 330–332 (2002) 262.
- [20] W. Li, Y.L. Du, Mater. Trans. 49 (2008) 2229.

- [21] F. Maurel, P. Leblanc, B. Knosp, M. Backhaus-Ricoult, J. Alloys Compd. 309 (2000) 88.
- [22] N. Cui, B. Luan, H.J. Zhao, H.K. Liu, S.X. Dou, J. Alloys Compd. 233 (1996) 236.
- [23] W. Zhang, Y. Zhu, C. Yang, L. Li, Int. J. Hydrogen Energy 35 (2010) 8241.
- [24] K. Young, M.A. Fetcenko, T. Ouchi, F. Li, J. Koch, J. Alloys Compd. 464 (2008) 238.
- [25] K. Young, M.A. Fetcenko, J. Koch, K. Morii, T. Shimizu, J. Alloys Compd. 486 (2009) 559.
- [26] W.J. Boettinger, D.E. Newbury, K. Wang, L.A. Bendersky, C. Chiu, U.R. Kattner, K. Young, B. Chao, Metall. Mater. Trans. A 41 (2010) 2033.
- [27] L.A. Bendersky, K. Wang, W.J. Boettinger, D.E. Newbury, K. Young, B. Chao, Metall. Mater. Trans. A 41 (2010) 1891.
- [28] L.A. Bendersky, K. Wang, W.J. Boettinger, D.E. Newbury, K. Young, B. Chao, Mater. Res. Soc. Symp. Proc. 1295, mrsf10-1295-n06-06.
- [29] K. Young, T. Ouchi, B. Huang, B. Chao, M.A. Fetcenko, L.A. Bendersky, K. Wang, C. Chiu, J. Alloys Compd. 506 (2010) 841.
- [30] K. Young, B. Huang, J. Yang, M.A. Fetcenko, Int. J. Hydrogen Energy 36 (2011) 11137.
- [31] K. Young, T. Ouchi, J. Nei, M.A. Fetcenko, Int. J. Hydrogen Energy 36 (2011) 11146.
- [32] Z. Shi, S. Chumbley, F.C. Laabs, J. Alloys Compd. 312 (2000) 41.
- [33] J.H. Zhu, P.K. Liaw, C.T. Liu, Mater. Sci. Eng. A 239–240 (1997) 260.
- [34] Nihon Kinzoku Gakkai, Hi Kagaku Ryouronteki Kinzoku Kagobutu, Maruzen, Tokyo, 1975, p. 296.
- [35] H.P. Klug, L.E. Alexander, X-ray Diffraction Procedures for Polycrystalline and Amorphous Materials, second ed. John Wiley & Sons, New York, 1974, p. 656.
- [36] T.B. Massalski, Binary Alloy Phase Diagram, ASM International, Ohio, USA, 1990.
- [37] A. Lindbaum, J. Hafner, E. Gratz, S. Heathman, J. Phys. Condens. Matter 10 (1998) 2933.
- [38] W.F. Gale, T.C. Totemeier, Smithells Metals Reference Book, eighth ed. Elsevier, Burlington, MA, 2004, 6–11.
- [39] R.L. Johnston, R. Hoffmann, Z. Anorg. Allg. Chem. 616 (1992) 105.
- [40] K. Kobayashi, K. Kanematsu, J. Phys. Soc. Jpn. 55 (1986) 1336.
- [41] K. Kobayashi, K. Kanematsu, J. Phys. Soc. Jpn. 55 (1986) 4435.
- [42] S. Katsuyama, R. Matsuo, M. Ito, J. Alloys Compd. 428 (2007) 262.
- [43] V.A. Romaka, R. Krayovskyy, L.P. Romaka, Bull. Natl. Lviv Polytechnic Univ. 639 (2009) 163 Available online: http://nbuv.gov.ua/portal/natural/VNULP/Avtomatyka/2009_639/23.pdf.
- [44] K. Young, B. Huang, J. Nei, M.A. Fetcenko, Int. J. Hydrogen Energy 36 (2011) 11146.
- [45] H. Okamoto, J. Phase Equilib. 16 (1995) 104.
- [46] H. Nakano, S. Wakao, I. Shimizu, J. Alloys Compd. 253–254 (1995) 609.
- [47] Y. Osumi, Suiso-kyuzo-goukin no Syurui to Sono, new ed., Agune Technology Center, Tokyo, Japan, 1999, p. 290.
- [48] Y. Osumi, Suiso-kyuzo-goukin no Syurui to Sono, new ed., Agune Technology Center, Tokyo, Japan, 1999, p. 57.
- [49] I. Aruna, L.K. Malhotra, B.R. Mehta, in: K.A. Gschneidner Jr., J.-C.G. Bünzli, V.K. Pecharsky (Eds.), Handbook on the Physics and Chemistry of Rare Earths, vol. 36, North-Holland, The Netherlands, 2006, p. 88.
- [50] K. Young, T. Ouchi, M.A. Fetcenko, J. Alloys Compd. 480 (2009) 428.
- [51] K. Young, T. Ouchi, W. Mays, B. Reichman, M.A. Fetcenko, J. Alloys Compd. 480 (2009) 434.
- [52] K. Young, T. Ouchi, M.A. Fetcenko, J. Alloys Compd. 480 (2009) 440.
- [53] K. Young, T. Ouchi, J. Koch, M.A. Fetcenko, J. Alloys Compd. 477 (2009) 749.
- [54] K. Young, T. Ouchi, M.A. Fetcenko, R.K. Regmi, G. Lawes, J. Alloys Compd. 490 (2010) 282.
- [55] K. Young, J. Nei, T. Ouchi, M.A. Fetcenko, J. Alloys Compd. 509 (2011) 2277.
- [56] F. Li, K. Young, T. Ouchi, M.A. Fetcenko, J. Alloys Compd. 471 (2009) 371.
- [57] K. Young, T. Ouchi, B. Huang, B. Reichman, M.A. Fetcenko, J. Power Sources 196 (2011) 8815.
- [58] K. Young, T. Ouchi, B. Huang, B. Reichman, M.A. Fetcenko, J. Power Sources 204 (2012) 205.
- [59] K. Young, T. Ouchi, B. Huang, B. Reichman, M.A. Fetcenko, Int. J. Hydrogen Energy 36 (2011) 12296.